RESEARCH ARTICLE | DECEMBER 11 2024

Drift kinetic electrostatic simulations of the edge localized mode heat pulse

V. I. Geyko ; I. Joseph ; M. A. Dorf ; D. Ghosh ; M. R. Dorr

Phys. Plasmas 31, 123903 (2024)
https://doi.org/10.1063/5.0230913

Drift kinetic electrostatic simulations of the edge localized mode heat pulse

Cite as: Phys. Plasmas **31**, 123903 (2024); doi: 10.1063/5.0230913
Submitted: 26 July 2024 · Accepted: 20 November 2024 ·
Published Online: 11 December 2024

V. I. Geyko,[a] I. Joseph, M. A. Dorf, D. Ghosh, and M. R. Dorr

AFFILIATIONS

Lawrence Livermore National Laboratory, Livermore, California 94550, USA

[a]Author to whom correspondence should be addressed: geyko1@llnl.gov

ABSTRACT

In the present work, electrostatic drift kinetic simulations of parallel plasma transport within the tokamak scrape-off layer (SOL) are conducted using the COGENT code. The SOL configuration is represented in one-dimensional slab geometry, incorporating a heat source localized in the midplane. The heat source parameters correspond to those characterizing edge-localized modes observed in the Joint European Torus (JET) tokamak. The numerical model includes kinetic treatment of both ions and electrons, a simplified model for the gyrokinetic Poisson equation that allows one to step over short time scales associated with fast electrostatic shear Alfvèn waves, and the logical sheath boundary condition (LSBC) that enforces global system quasineutrality. A third-order accurate LSBC is derived to be consistent with the third-order accurate upwind advection scheme utilized in the code, and it was shown to noticeably impact the simulation results, especially parallel heat flux at the target plate. The findings of this study are in agreement with results from preceding fluid and kinetic simulations.

I. INTRODUCTION

Tokamak fusion reactors, operating under high-performance H-mode[1,2] conditions, are susceptible to the occurrence of edge-localized mode instabilities.[3,4] These instabilities have the potential to rapidly expel hot plasma into the scrape-off layer (SOL).[5–7] The resulting energetic particles, which follow trajectories parallel to the magnetic field lines within the scrape-off layer, can lead to significant energy deposition onto the plasma-facing components (PFCs). This deposition, in turn, can trigger erosion, damage, and the release of impurities into the core plasma.[8,9] Accurate numerical simulations of the heat pulse propagation and the total power load to the PFCs hold pivotal importance for both theoretical studies aimed at comprehending underlying physical phenomena, as well as future experimental planning efforts.

A rigorous numerical analysis of the heat pulse propagation caused by edge-localized modes (ELMs) in the scrape-off layer of a tokamak necessitates simulations of plasma turbulence in a curved tokamak geometry, encompassing both parallel and perpendicular plasma transport as well as integrated ELM modeling.[10,11] However, the complexity of this problem often leads to its treatment in a simplified manner. A test case, derived from experiments conducted on the JET,[12] involving the propagation of an ELM-induced heat pulse along the SOL to a divertor target plate, has been used as a benchmark in recent literature. This test case is confined to a single spatial dimension and models an ELM as an intense heat source near the midplane without directly simulating the magnetohydrodynamic instabilities and reconnection processes that drive the ELM. Despite these simplifications, this approach is valuable for testing simulation codes and gaining insights into the physics of parallel heat propagation and divertor heat fluxes.

Early investigations by Bergmann[13] using a 1D1V particle-in-cell (PIC) code revealed a sharp spike in the electron heat flux on the target plate immediately following the ELM crash, accompanied by a rapid increase in sheath potential. These studies indicated that the electron contribution to the total target heat flux was minimal. Takizuka[14] later employed a 1D2V PIC model for electrons and a 1D3V model for ions, confirming similar results. However, in the collisionless limit, the initial spike in electron heat flux was significantly greater. It is noteworthy that the plasma parameters used in these studies differed from those in the JET experiment that was later fixed by Pitts.[7] In 1D1V PIC simulations that Pitts performed, the electron contribution was around 30% of the total ELM energy, with results aligning well with experimental observations.

Various numerical tools have been utilized to address this problem, including 1.5D3V PIC simulations,[15] a Vlasov–Poisson model,[16] and the BOUT++ framework,[17] which enabled comparisons between non-local and diffusive heat flux models for the scrape-off layer.

A comprehensive benchmark of fluid, Vlasov, and PIC approaches to this problem was compiled by Havlíčková,[18] where it was noted that fluid models lacked a fast kinetic electron response for the parallel heat flux. Of particular interest for the present work are the gyrokinetic simulations conducted using the Gkeyll[19] and GENE[20] codes, which have demonstrated consistency with the results from PIC and Vlasov kinetic models.[18] Both studies employed identical simulation setups, boundary conditions, and models for the electrostatic potential, making them excellent benchmarks for comparison.

The problem was later revisited using the gyrokinetic COGENT code,[21] which employed magnetized kinetic ions and a simplified Boltzmann electron model. Despite yielding results that qualitatively aligned with earlier kinetic and fluid modeling investigations, these outcomes omitted important electron kinetic effects. Notably absent was the swift spike in the parallel heat flux observed during transit electron times, a phenomenon previously documented in prior studies.[18–20] This discrepancy prompted a motivated effort to enhance the existing model by introducing magnetized kinetic electrons into the framework. In order to ensure a consistent and equitable comparison, we opted to adopt the test case established by Pitts[7] and repeated by other authors. In particular, our model assumes one-dimensional (1D) geometry and the ELM heat pulse that is represented as a source of hot particles in the midplane. It also includes the logical sheath boundary condition (LSBC) for electrons to ensure global charge conservation and an algebraic model for the electrostatic potential (see works of Shi[19] and Pan[20]) to mitigate severe computational constraints of fast electrostatic Alfvèn waves. In this study, we conduct a comprehensive analysis of the latter two issues, resulting in several key findings.

The algebraic model for the electrostatic potential is governed by a dimensionless parameter $(k\rho)_0^2$, which quantifies the strength of the potential response to local deviations from charge quasineutrality (see Sec. III C). Although this model has been widely adopted in the literature, a comprehensive validation has not been performed to the best of the authors' knowledge. Specifically, the appropriate value for the parameter $(k\rho)_0^2$ required to ensure both efficient simulations and reliable results has remained uncertain. We tested this model by studying the propagation of electrostatic shear Alfvèn waves and identified a finite range of the $(k\rho)_0^2$ parameter that is optimal for accelerating simulations while maintaining an adequate level of charge quasineutrality. We tested different advection schemes and demonstrated that the first-order upwinding method was unusable over system time scales determined by ion transit times. This advection method caused excessive numerical heating of electrons, yielding unphysical simulation results. To address this issue, we employed a third-order advection scheme and developed the logical sheath boundary condition consistent with the order of the advection method. Additionally, we demonstrated that conducting simulations with finite collisionality is preferable for achieving optimal results, since collisions help to mitigate numerical artifacts, such as Gibbs oscillations, which are present when using high-order advection methods.

The paper is organized as follows. Basic equations and geometry are described in Sec. II. The gyrokinetic Poisson equation (GPE) and the algebraic model for the electrostatic potential are discussed in Sec. III. Implementation of the LSBC is derived in Sec. IV. Simulation setup and results are provided in Sec. V. Finally, we summarize our results in Sec. VI and discuss possible future improvements.

II. PROBLEM FORMULATION

A. Geometry

Simulations encompassing the propagation of ELM heat pulses have been executed employing the established test case configuration from preceding studies.[18–21] The intricate geometry inherent to the tokamak scrape-off-layer is substituted with a simplified 1D slab geometry. In this setup, all quantities exhibit variations solely in the poloidal $\hat{\mathbf{y}}$ direction. The magnetic field denoted as $\mathbf{B}$ remains constant in space and time, and it forms an angle θ with the toroidal direction $\hat{\mathbf{z}}$; thus, it reads as

$$\mathbf{B} = B_0\hat{\mathbf{b}} = B_0(\hat{\mathbf{x}}\cos(\theta) + \hat{\mathbf{y}}\sin(\theta)), \tag{1}$$

where B_0 is the amplitude, and $\hat{\mathbf{b}}$ is the unit vector in parallel direction, i.e., along the magnetic field line. The simulation domain spans in the poloidal direction from $-L_y$ to L_y where the divertor target plates are located. The domain length is related to the connection length of the scrape-off-layer L as $2L_y = \sin(\theta)L$. The ELM heat pulse is represented as a symmetric steady state source of hot particles with the scale L_s in $\hat{\mathbf{y}}$ direction acting for 200 μs (see details in Sec. V A). The schematics of the problem geometry are shown in Fig. 1.

Owing to the design of the COGENT code, we have to consider a two-dimensional (2D) problem with no dynamics and uniform distribution of all physical quantities in the perpendicular $\hat{\mathbf{x}}$ direction. We use four cells in the $\hat{\mathbf{x}}$ direction, which correspondingly slow down the performance of our simulations. While our current work is focused on removing this design limitation, it serves as a reliable means to demonstrate the absence of perpendicular dynamics and validate the applicability of the assumed 1D model.

B. Gyrokinetic formulation

The finite volume continuum gyrokinetic code COGENT solves for time evolution of the full gyrokinetic probability distribution function (PDF) $f_\alpha(\mathbf{R}, v_\parallel, \mu)$ for species α,

$$\frac{\partial g_\alpha}{\partial t} + \nabla_{\mathbf{R}}\cdot\left(\dot{\mathbf{R}}_\alpha g_\alpha\right) + \frac{\partial}{\partial v_\parallel}\left(\dot{v}_{\parallel\alpha} g_\alpha\right) = \bar{S} + \bar{C}. \tag{2}$$

Here, $\mathbf{R}$ is the particle guiding center coordinate; hence, $\nabla_{\mathbf{R}}$ is the differential operator with respect to $\mathbf{R}$; $v_\parallel$ is the parallel velocity of the

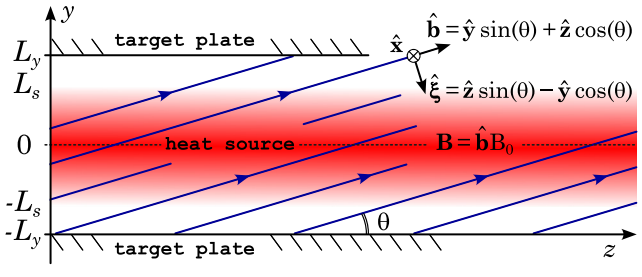

FIG. 1. Illustration of the one-dimensional slab geometry used in the simulations. Here, unit vectors $(\hat{\mathbf{x}}, \hat{\mathbf{y}}, \hat{\mathbf{z}})$ form an orthogonal basis, where $\hat{\mathbf{y}}$ correspond to the poloidal and $\hat{\mathbf{z}}$ to the toroidal directions of the tokamak. Another basis is made of unit vectors $(\hat{\mathbf{x}}, \hat{\mathbf{b}}, \hat{\boldsymbol{\xi}})$, where $\hat{\mathbf{b}}$ is a vector in the direction parallel to the magnetic field $\mathbf{B}$ and it makes an angle θ with $\hat{\mathbf{z}}$. Unit vector $\hat{\boldsymbol{\xi}}$ is orthogonal to both $\hat{\mathbf{x}}$ and $\hat{\mathbf{b}}$. The domain is limited in y-direction by divertor target plates at $\pm L_y$, and the heat source that represents the ELM pulse is located in the midplane at $-L_s < y < L_s$.

particle, i.e., the velocity of free streaming along the magnetic field line direction $\hat{\mathbf{b}}$; $\mu = m_\alpha v_\perp^2/2B$ is the magnetic moment, which is conserved in the gyrokinetic approximation; q_α and m_α are the particle charge and mass, respectively, $g_\alpha = B_{\parallel\alpha}^* f_\alpha$ is the distribution function multiplied by the Jacobian of the transformation to the gyrokinetic variables,[22] with

$$\mathbf{B}^* = B + \frac{c v_\parallel m_\alpha}{q_\alpha} \nabla \times \hat{\mathbf{b}}, \tag{3}$$

and c is the speed of light in vacuum. On the right hand side (RHS) of Eq. (2), $\bar{S} = S(\mathbf{R}, v_\parallel, \mu, t)$ is the source function, and $\bar{C} = C[f_\alpha, f_\alpha]$ is the collision operator with only like-species collisions employed in this work. In the collisionless and sourceless case, the evolution of the PDF is a pure advection in the reduced phase space $\mathbb{R} = \{\mathbf{R}, v_\parallel, \mu\}$. Adopting the geometry of the problem from Sec. II A, one obtains the guiding center velocity,

$$\begin{aligned}\dot{\mathbf{R}} &= \hat{\mathbf{b}} v_\parallel + \hat{\mathbf{x}} c \frac{E_y B_z}{B^2} - \hat{\mathbf{y}} c \frac{E_x B_z}{B^2} + \hat{\mathbf{z}} c \frac{E_x B_y}{B^2} \\ &= \hat{\mathbf{b}} v_\parallel + \hat{\mathbf{x}} c \frac{E_y B_z}{B^2}.\end{aligned} \tag{4}$$

All terms that contain E_x vanish due to the 1D nature of the problem, and the last term $\hat{\mathbf{x}} c \frac{E_y B_z}{B^2}$ represents a uniform $E \times B$ drift. In Eq. (3), $\nabla \times \hat{\mathbf{b}} = 0$, therefore $B^* = B_0$ and the only difference between f_α and g_α is the scaling factor B_0. Projections of the vector $\hat{\mathbf{b}}$ to $\hat{\mathbf{y}}$ and $\mathbf{E}$ to $\hat{\mathbf{b}}$ both yield a factor of $\sin(\theta)$, as follows from Eq. (1), thus, the modified Eq. (2) reads as

$$\frac{\partial f_\alpha}{\partial t} + v_\parallel \sin(\theta) \frac{\partial f_\alpha}{\partial y} + \frac{q_\alpha E_y \sin(\theta)}{m_\alpha} \frac{\partial f_\alpha}{\partial v_\parallel} = S + C, \tag{5}$$

where the source and collision terms are rescaled as $B_0 S = \bar{S}$ and $B_0 C = \bar{C}$.

Equation (5) combined with the gyrokinetic Poisson equation (GPE) forms the gyrokinetic formalism that describes the orbit-averaged motion of magnetized particles. This formalism generally incorporates low-order drift terms and higher-order gyro-terms, such as phase averaging and polarization correction in the GPE.[23] However, due to the simplicity of the geometry adopted in this study and the algebraic model for the Poisson equation detailed in Sec. III C, the current formalism reduces to drift kinetics, thereby justifying the title of this work.

III. ELECTROSTATIC POTENTIAL

A. Gyrokinetic Poisson equation

The electrostatic gyrokinetic equation Eq. (5) requires the electric field, which is obtained through the solution of the gyrokinetic Poisson equation[24] for the potential ϕ

$$q(n_i - n_e) = -\frac{\nabla^2 \phi}{4\pi} - \sum_\alpha \nabla_\perp \cdot \left(\frac{q_\alpha^2 n_\alpha}{m_\alpha \Omega_{c,\alpha}^2} \nabla_\perp \phi \right), \tag{6}$$

and

$$\mathbf{E} = -\hat{\mathbf{y}} \frac{\partial \phi}{\partial y}. \tag{7}$$

Here, $\Omega_{c,\alpha}$ is the cyclotron frequency given by $\Omega_{c,\alpha} = q_\alpha B/(m_\alpha c)$ and the sum over species in the right hand side (RHS) of Eq. (6) has electron and ion terms. The electron contribution can be neglected, since for $n_e \approx n_i$ and for $q = q_i = -q_e$ assuming two species plasma with singly ionized ions we obtain

$$\begin{aligned}\frac{q_i^2 n_i}{m_i \Omega_{c,i}^2} &= \frac{q^2 n_i m_i^2 c^2}{m_i q^2 B^2} \\ &= \frac{m_i}{m_e} \frac{q^2 n_e m_e^2 c^2}{m_e q^2 B^2} = \frac{m_i}{m_e} \left(\frac{q_e^2 n_e}{m_e \Omega_{c,e}^2} \right) \gg \frac{q_e^2 n_e}{m_e \Omega_{c,e}^2}.\end{aligned} \tag{8}$$

The first term in the RHS of Eq. (6) corresponds to the vacuum part of Poisson equation, while the last term is the polarization correction. The last term is dominant since

$$\frac{4\pi q_i^2 n_i}{m_i} \frac{m_i^2 c^2}{q^2 B_0^2} = \frac{c^2}{V_A^2} \gg 1, \tag{9}$$

where $V_A^2 = B_0^2/(4\pi m_i n_i)$ is the Alfvèn velocity, and for the parameters of simulations provided in Table I, $c^2/V_A^2 \approx 2 \cdot 10^3 \gg 1$; therefore, the vacuum term can be omitted.

The differential operator in the last term of Eq. (6) is perpendicular to the magnetic field direction $\hat{\mathbf{b}}$. In a different orthogonal coordinate system $(\hat{\mathbf{x}}, \hat{\mathbf{b}}, \hat{\boldsymbol{\xi}})$ shown in Fig. 1, $\hat{\boldsymbol{\xi}} = \hat{\mathbf{z}} \sin(\theta) - \hat{\mathbf{y}} \cos(\theta)$; hence, the perpendicular gradient of the potential is simplified to $\nabla_\perp \phi = -\hat{\boldsymbol{\xi}} \frac{\partial \phi}{\partial \xi}$ and the divergence operator is given by

$$\frac{m_i c^2}{B^2} \nabla_\perp \cdot (n_i \nabla_\perp \phi) = \frac{m_i c^2}{B_0^2} \frac{\partial}{\partial \xi} \left(n_i \frac{\partial \phi}{\partial \xi} \right). \tag{10}$$

Following the chain rule, one obtains

TABLE I. Parameters of the simulations. Here, n_0, T_0, L_0, and V_0 are COGENT normalization units for density, temperature, length, and velocity, respectively.

Description	Label	Value
Density normalization	n_0	10^{13} cm^{-3}
Temperature normalization	T_0	100 eV
Magnetic field	B_0	3 T
Magnetic field angle	θ	0.1047 rad
Mass normalization	m_0	$1.673 \cdot 10^{-24}$ g
Velocity normalization	$V_0 = \sqrt{\frac{T_0}{m_0}}$	$9.796 \cdot 10^6$ cm/s
Ion thermal velocity	$V_{ti} = V_0 \sqrt{\frac{m_0}{m_i}}$	$6.927 \cdot 10^6$ cm/s
Electron thermal velocity	$V_{te} = V_0 \sqrt{\frac{m_0}{m_e}}$	$4.197 \cdot 10^8$ cm/s
Alfvèn velocity	$V_A = \frac{B_0}{\sqrt{4\pi m_i n_0}}$	$1.463 \cdot 10^9$ cm/s
Parallel connection length	L	8000 cm
Length normalization	$L_0 = L \sin(\theta)$	836.2277 cm
Source length	L_s	130.661 cm
Ion cyclotron freq.	$\Omega_{ci} = \frac{qB_0}{2cm_0}$	$1.436 \cdot 10^8$ s^{-1}
Electron cyclotron freq.	$\Omega_{ce} = \frac{qB_0}{cm_e}$	$5.273 \cdot 10^{11}$ s^{-1}
Ion gyroradius	$\rho_i = V_{ti}/\Omega_{ci}$	$4.824 \cdot 10^{-2}$ cm
Electron gyroradius	$\rho_e = V_{te}/\Omega_{ce}$	$7.959 \cdot 10^{-4}$ cm

$$\frac{\partial}{\partial \xi} = \frac{\partial y}{\partial \xi}\frac{\partial}{\partial y} + \frac{\partial z}{\partial \xi}\frac{\partial}{\partial z} = \frac{\partial y}{\partial \xi}\frac{\partial}{\partial y} = -\cos(\theta)\frac{\partial}{\partial y}, \tag{11}$$

and the gyrokinetic Poisson equation is transformed to the following:

$$0 = (n_i - n_e) + \frac{m_i c^2}{qB_0^2}\cos^2(\theta)\frac{\partial}{\partial y}\left(n_i \frac{\partial \phi}{\partial y}\right). \tag{12}$$

B. Linear analysis

In this section, we derive and analyze the dispersion relation for linear perturbations in the system of Eqs. (5) and (12). The sourceless equilibrium solution ($\frac{\partial}{\partial t} = 0$) of Eq. (5) is an arbitrary smooth function of $(m_\alpha v_\parallel^2/2 + q\phi)$, where $E_y = -\frac{\partial \phi}{\partial y}$. Based on the natural assumption of Maxwellian equilibrium solution, we find the dispersion relation using linear perturbation theory. In particular, consider small oscillating perturbations of the potential $\tilde{\phi}$ and the distribution function $\tilde{f}_\alpha$ characterized by frequency ω and wave vector k_y,

$$\phi = \tilde{\phi}\exp(-i\omega t + ik_y y), \tag{13}$$

$$f_\alpha = n_0\left(\frac{m_\alpha}{2\pi T_\alpha}\right)^{3/2}\exp\left(-\frac{m_\alpha v_\parallel^2}{2T_\alpha} - \frac{\mu_\alpha B}{T_\alpha}\right) + \tilde{f}_\alpha \exp(-i\omega t + ik_y y). \tag{14}$$

Assuming stationary ions and making use of the relation $\tilde{E}_y = -ik_y\tilde{\phi}$, substitute the perturbation of the electron distribution function from Eq. (14) into Eq. (5)

$$-i\bar{\omega}\sin(\theta)\tilde{f}_e + ik_y\tilde{f}_e v_\parallel \sin(\theta) + \frac{ik_y q\tilde{\phi}\sin(\theta)}{m_e}\frac{\partial f_{0,e}}{\partial v_\parallel} = 0, \tag{15}$$

where $\bar{\omega} = \omega/\sin(\theta)$. In the limit $\bar{\omega} \gg k_y v_\parallel$, the plasma dispersion function can be Taylor expanded; thus, the expression for the perturbed density reads as

$$\tilde{n}_e = \int_{v_\parallel,\mu} dv_\parallel d\mu \tilde{f} = \frac{q\tilde{\phi}k_y}{m_e}\int_{v_\parallel,\mu} dv_\parallel d\mu \frac{\frac{\partial f_{0,e}}{\partial v_\parallel}}{\bar{\omega} - k_y v_\parallel} \approx \frac{q\tilde{\phi}k_y}{\bar{\omega}m_e}\int_{v_\parallel,\mu} dv_\parallel d\mu \frac{\partial f_{0,e}}{\partial v_\parallel}\left(1 + \frac{k_y v_\parallel}{\bar{\omega}}\right) \approx -\frac{q\tilde{\phi}k_y^2 n_0}{\bar{\omega}^2 m_e}. \tag{16}$$

Finally, $\tilde{n}_e$ from Eq. (16) and the gyrokinetic Poisson equation Eq. (12) yield the dispersion relation for linear waves

$$\omega^2 = \frac{m_i}{m_e}\Omega_{c,i}^2 \cdot \frac{(\sin(\theta)k_y)^2}{(\cos(\theta)k_y)^2} = \frac{V_{te}^2 k_\parallel^2}{\rho_s^2 k_\perp^2}. \tag{17}$$

Here, V_{te} is the electron thermal velocity $V_{te}^2 = T_e/m_e$, T_e is the characteristic electron temperature, $k_\perp = \cos(\theta)k_y$, $k_\parallel = \sin(\theta)k_y$, and $\rho_s^2 = T_e/(m_i\Omega_{c,i})$ is the ion gyroradius.

The dispersion relation in Eq. (17) is the electrostatic limit of the shear Alfvén waves[25–27] (ESAWs). The right-hand-side of Eq. (17) is written in the way it widely appears in the literature where it is typically argued[19] that the frequency can become very large for small $k_\perp\rho_s$ (for example the smallest possible $k_\perp$ resolved on the computational grid); thus, the numerical stability of simulations should be considered carefully, once these type of waves emerge. As a result, a tight time step constraint[25] such as $\Delta t\omega \lesssim 1$ should be enforced. The issue is mitigated in the electromagnetic formulation, as the perturbations from the vector potential $A_\parallel$ yield an additional term[28] in the denominator in Eq. (17), in particular $k_\perp^2 \to k_\perp^2 + \omega_{pe}^2/c^2$, where $\omega_{pe}^2 = 4\pi q^2 n_e/m_e$ is the electron plasma frequency. Notice, however, that in the present 1D slab geometry, parallel and perpendicular components of the wave vector are related to each other; therefore, the argument of large ω at small $k_\perp$ is not valid. Instead, the frequency does not depend on k_y at all and equals $\omega = \Omega_{ci}\tan(\theta)(m_i/m_e)^{1/2}$. For the parameters of the simulations (see Table I), $\tan(\theta) = 0.1051$, $m_i/m_e = 3670.5$, thus, $\omega = 6.37\Omega_{ci}$. Even though ω does not grow unboundedly large for $k_\perp \to 0$, the values greater than the ion cyclotron frequency eliminate the benefits of the gyrokinetic approximation. In order to mediate this issue, we adopt an algebraic potential model employed in Refs. 19 and 20 that imposes a lower bound limit on $k_\perp$ in the denominator on the right hand side of Eq. (17). It is worth mentioning that using V_{te} and ρ_s in Eq. (17) might be confusing, since both these quantities depend on ambiguous electron temperature that varies in space and time during simulations. Instead, it is better to use the COGENT normalization temperature T_0 so that $V_{te,0} = T_0/m_e$ and $\rho_0^2 = T_0/(m_i\Omega_{c,i})$ where both are constants and have the meaning of the characteristic electron temperature and ion gyroradius.

C. Algebraic model for the potential

The algebraic model for the electrostatic potential was used in gyrokinetic simulations conducted by Shi[19] and Pan.[20] The fundamental concept behind this model is the substitution of the differential operator in Eq. (12) with a predetermined constant value. Although this model was utilized in simulations and yielded reasonably satisfactory outcomes, it warrants more thorough examination and scrutiny. In this context, we revisit the model, subjecting it to a more detailed and rigorous examination to better understand its suitability and applicability.

The gyrokinetic Poisson equation [Eq. (12)] in dimensionless units reads as

$$0 = (\bar{n}_i - \bar{n}_e) + \frac{T_0}{m_i}\cdot\frac{m_i^2 c^2}{q^2 B_0^2}\cdot\frac{\cos^2(\theta)}{L_0^2}\frac{\partial}{\partial \bar{y}}\left(\bar{n}_i\frac{\partial \bar{\phi}}{\partial \bar{y}}\right), \tag{18}$$

where normalizations are given in Table I such that $\bar{n}_\alpha = n_\alpha/n_0$, $\bar{y} = y/L_0$, $\bar{\phi} = q\phi/T_0$. Assuming for demonstration purposes that the ion density $\bar{n}_i$ inside the differential operator on the right-hand-side of Eq. (18) is constant, the equation can be analyzed in Fourier space where all quantities Z are represented as a sum of harmonics $\bar{Z} = \sum_{k_y} Z_{k_y} e^{+iyk_y}$ with complex amplitudes Z_{k_y}. The relation between $\bar{\phi}_k$ and the charge density $\bar{n}_{ik} - \bar{n}_{ek}$ is given by

$$\frac{(\bar{n}_{ki} - \bar{n}_{ke})}{\bar{n}_i} = \frac{T_0}{m_i}\cdot\frac{m_i^2 c^2}{q^2 B_0^2}\cdot\frac{\cos^2(\theta)\bar{k}_y^2}{L_0^2}\bar{\phi}_k. \tag{19}$$

The denominator on the left-hand-side of Eq. (19) contains the ion density that is assumed to be constant; thus, the subscript k is omitted. The numerical coefficient in front of $\bar{\phi}_k$ characterizes the potential response to the charge density variations, and this response is lower

for higher k_y modes. We denote this coefficient as $(k\rho)_0^2$, and it can be viewed as the product of the ion gyroradius and some k_y since

$$(k\rho)_0^2 = \frac{T_0}{m_i}\cdot\frac{m_i^2c^2}{q^2B_0^2}\cdot\frac{\cos^2(\theta)\bar{k}_y^2}{L_0^2} = \frac{V_{ti,0}^2}{\Omega_{ci}^2}\cdot\frac{\cos^2(\theta)\bar{k}_y^2}{L_0^2} = \frac{V_{ti,0}^2}{\Omega_{ci}^2}k_\perp^2 = (\rho_{i,0}k_\perp)^2. \tag{20}$$

Ignoring the constant potential shift, i.e., $\bar{k}_y = 0$ mode, the smallest $\bar{k}_y$ resolved in the simulations (corresponding to a half of wavelength) is $\bar{k}_y = \pi/2$, which corresponds to one half of the wavelength. The largest $\bar{k}_y$ is the Nyquist frequency, namely, $\bar{k}_y = \pi N_y$ for a grid with N_y computational cells. For the parameters of simulations from Table I and $N_y = 128$ that was used for the production runs, we obtain

$$\begin{aligned}(k\rho)_{0,\min}^2 &= 8.207\cdot10^{-9},\\ (k\rho)_{0,\max}^2 &= 5.379\cdot10^{-4}.\end{aligned} \tag{21}$$

According to the design of the algebraic potential model, the coefficient $(k\rho)_0^2$ is a constant in space and time; therefore, going back from Fourier to coordinate space, the reduced GPE reads as

$$\frac{\bar{n}_i - \bar{n}_e}{\bar{n}_i} = (k\rho)_0^2\bar{\phi}. \tag{22}$$

The most natural idea is to choose the parameter $(k\rho)_0^2$ such that it corresponds to the dominant value of $\bar{k}_y$ in the spectrum of $\bar{\phi}$. However, for smooth profiles of the initial plasma parameters and the ELM heat source, $\bar{k}_y$ is close to $\bar{k}_{y,\min}$; hence, $(k\rho)_0^2$ is very small implying that there are no dominant modes with high $\bar{k}_y$ in the Fourier spectrum. That in turn imposes strict constraints on the time step and eliminates the premise of using the algebraic model at all. On the other hand, in the case of unphysically large $(k\rho)_0^2$, the local charge quasineutrality is not established, since the potential and electric field response are too weak. In order to select the proper value of the $(k\rho)_0^2$ parameter, we identify the following desired requirements:

- Convergence. The results of the simulations should not vary noticeably when the parameter $(k\rho)_0^2$ is changed by an order of magnitude. The results here are assumed to be some global observations, for example, the total parallel heat flux on the target plate. We ignore small scale noise-like effects such as ESAW beating. The stability of the results does not necessarily guarantee the correctness; however, in the opposite case, the model cannot yield quantitatively reliable results, since there is no distinguished value of $(k\rho)_0^2$.
- Time step constraint. Using the explicit Runge–Kutta time integration scheme, the time step is limited by the Courant–Friedrichs–Lewy (CFL) constraint.[29] Skipping some complicated algebra that leads to corrections based on the advection scheme, the maximum time step scales as $\Delta t = \min[\Delta y/v_y]$. Typically, for a fixed computational grid, hence fixed Δy, the maximum velocity is determined by super thermal electrons. However, at some small $(k\rho)_0^2$, the phase velocity of the ESAW can become faster; therefore, the maximum time step is dominated by the Alfvén wave. Our objective is to minimize or altogether circumvent such situations to enhance computational efficiency.

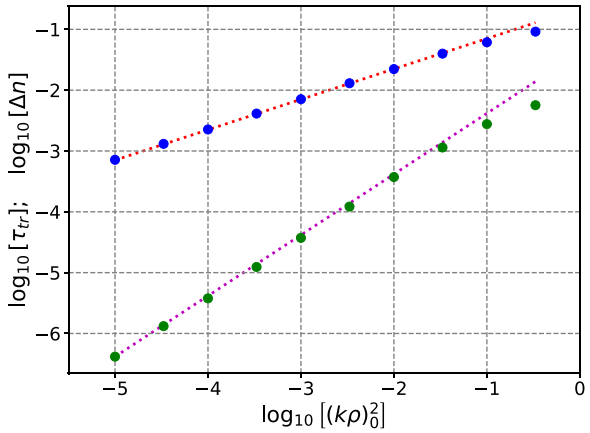

FIG. 2. Logarithmic plots of the normalized transit time $\tau_{tr} = V_0/V_{ph}$ and normalized maximum charge density Δn as a function of the $(k\rho)_0^2$ parameter. Blue dots: measured τ_{tr}. Red dotted line: Analytic result from Eq. (24). Green dots: measured Δn. Magenta dotted line: linear approximation of the measured data.

- Quasineutrality. Ideally, we would like to keep local charge quasineutrality on the same level as the original gyrokinetic Poisson equation does, which is not possible if large $(k\rho)_0^2$ values are used. Nonetheless, it is important to note that the total charge of the system may not be conserved precisely throughout the simulations. Factors contributing to this deviation could include leakage of the distribution function through the upper velocity boundary of the computational domain or imperfections in the boundary conditions. If the code can accommodate a certain degree of global quasineutrality violation, we may anticipate that local quasineutrality would be similarly affected, potentially establishing a threshold value permissible within the algebraic model. Figure 2 demonstrates how the maximum difference $(\bar{n}_i - \bar{n}_e)$ during a test run depends on $(k\rho)_0^2$. Local quasineutrality of 1% is achieved at $(k\rho)_0^2 = 0.333$.
- Resolution of ESAWs. By incorporating the algebraic model for the electrostatic potential into the framework, the dispersion relation presented in Eq. (17) undergoes the following modifications:

$$\omega^2 = \frac{T_0}{m_e}\frac{\sin^2(\theta)k_y^2}{(k\rho)_0^2} = \frac{k_y^2V_{te,0}^2\sin^2(\theta)}{(k\rho)_0^2}, \tag{23}$$

where $V_{te,0} = \sqrt{T_0/m_e}$. The phase velocity of the electrostatic shear Alfvén wave is determined as

$$V_{ph} = \frac{\omega}{k_y} = \frac{V_{te,0}\sin(\theta)}{(k\rho)_0}, \tag{24}$$

so it is constant for all wavelengths unlike the original gyrokinetic Vlasov–Poisson model where it is infinite for $k_\perp \to 0$ as follows from Eq. (17). The parameter $(k\rho)_0^2$ should be chosen in such a way that the ESAW is resolved in simulations.

We conducted an analysis of the appropriateness of the algebraic model, taking into account the specified criteria mentioned above. To assess its suitability, we designed a specialized test case involving a collisionless plasma comprised of deuterium ions and electrons. This plasma contained no additional sources and was simulated within a

1D geometry framework, characterized by the constant magnetic field as described in Sec. II A. The ESAW was seeded by the initial profiles for normalized densities and temperature of ions and electrons,

$$\bar{n}_{i,e} = 1.0 + 0.02\exp\left(-\pi^2(\bar{y}-0.5)^2\right),$$
$$\bar{T}_{i,e} = 1.0,$$
$$\bar{y} \in [0,1].$$

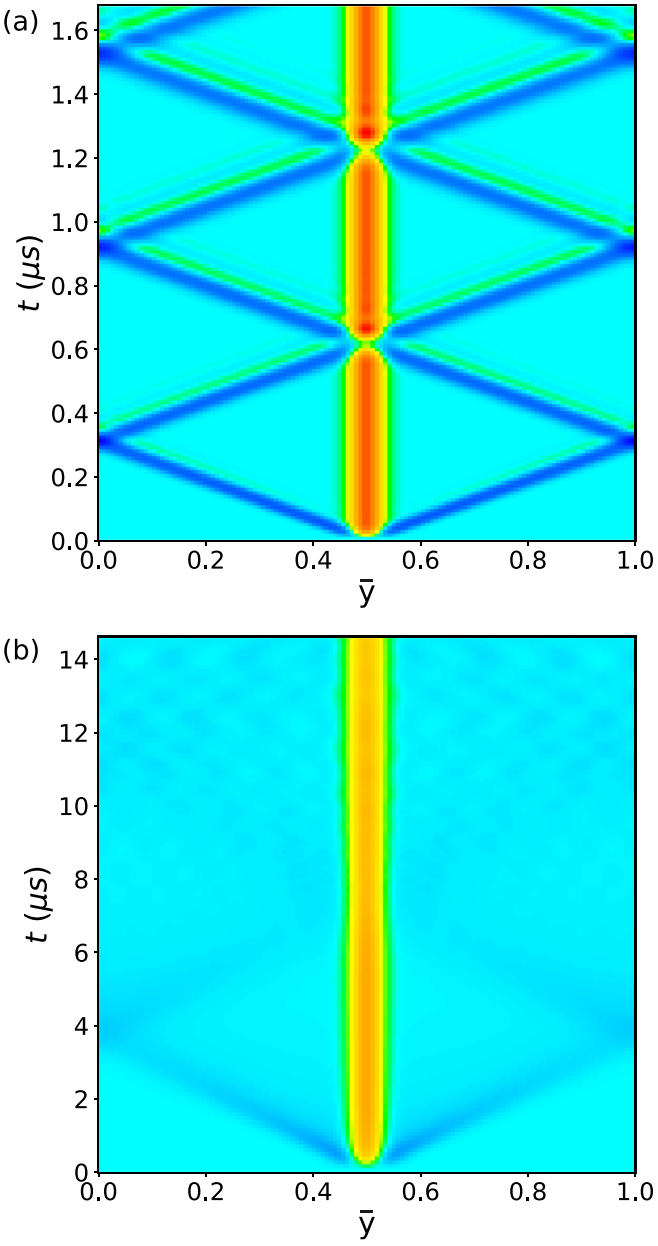

FIG. 3. Time evolution of the potential plot resolved for (a) $(k\rho)_0^2 = 0.001$, and (b) $(k\rho)_0^2 = 0.333$. The top figure demonstrates clear signature of ESAWs propagating in the domain and bouncing/penetrating the walls. The bottom figure shows fast dissipation of the wave and smearing of the structure.

At the beginning of the simulations, fast electrons in the density bump stream away from the midplane at $\bar{y} = 0.5$ that creates charge imbalance and launches ESAWs. The waves propagate with the phase velocity given in Eq. (24) toward to the boundaries of the simulation domain and reappear on the opposite side as the periodic boundary conditions are used. In these test runs, we collected statistics on how the transit time of the waves $\tau = L_0/V_{ph}$ and the maximum charge density Δn depend on the parameter $(k\rho)_0^2$. We also studied how the critical time step that determines stability of the simulations depends on $(k\rho)_0^2$. The results of the simulations are visualized in Fig. 2. Normalized transit time τ_{tr} is measured by approximating tracers of the ESAWs (vivid diagonal lines in the top plot of Fig. 3) by straight lines and by measuring the time it takes such a straight tracer to cross the computational domain. It is then compared to the normalized analytical expression that follows from Eq. (24):

$$\tau_a = \frac{L_0}{V_{ph}}\frac{V_0}{L_0} = \frac{m_0}{m_e}\frac{\sin(\theta)}{(k\rho)_0}, \tag{25}$$

and it was shown to be in good agreement for all values of $(k\rho)_0^2$ less than 0.1. The wave structure for $(k\rho)_0^2 = 0.1$ and greater gets smeared out quickly, which is depicted in the bottom plot of Fig. 3. In fact, the dispersion relation in Eq. (17) is no longer valid since it was derived under the assumption $\omega \gg k_y v_\parallel \sin(\theta)$. Substituting ω from Eq. (23) and assuming that $v_\parallel \sim V_{te}$, the applicability condition reads as $(k\rho)_0^2 \ll 1$ that is not satisfied for $(k\rho)_0^2 \geq 0.1$. The maximum charge density Δn is defined as the maximum value of $(\bar{n}_i - \bar{n}_e)$ over all the domain and simulation time. It was observed that this difference is always greatest at the very early stage of the simulations when the wave gets launched. A plausible explanation of this observation is that the wave eventually decays due to numerical dissipation and Landau damping. We do not obtain an analytical scaling for Δn from the algebraic potential model; however, based on the measured data, it is possible to conclude that $\Delta n \sim (k\rho)_0^2$, and this scaling is valid again for $(k\rho)_0^2 \leq 0.1$.

Results of the critical CFL number as a function of $(k\rho)_0^2$ are shown in Table II. The critical CFL number determines the critical time step when the code becomes unstable. The time step calculated as a product of the base time step and the CFL number, where the base time step is determined by the smallest ratio $\Delta y/v_y$, thus, by the fastest electrons resolved by the code as the space grid step Δy is fixed. In the absence of ESAWs, the code typically runs with CFL = 1.0 even though theoretically it can run even faster as the stability constraint contains extra numerical factors that depend on the dimensionality of the problem and on the advection scheme used. Skipping these details, we conclude that the critical value of the $(k\rho)_0^2$ parameter is 0.00333 when the critical CFL number is 0.975, which is almost equal to unity. In this context, the phase velocity of the waves reaches such high values

TABLE II. Critical CFL number for the COGENT time step as a function of the $(k\rho)_0^2$ parameter. CFL = 1.0 for all $(k\rho)_0^2 > 0.0333$ that implies that the time step is limited by the fast electron dynamics instead of ESAWs.

$(k\rho)_0^2$	1×10^{-5}	3.3×10^{-5}	1×10^{-4}	3.33×10^{-4}	0.001	0.00333	0.01
CFL	0.0528	0.096	0.165	0.305	0.535	0.975	1.0

that it begins to influence the stability of the code. Therefore, selecting a value of $(k\rho)_0^2 \geq 0.00333$ is advantageous to attain the fastest possible simulation speed. Taking into consideration all the criteria we discussed, the optimal range for $(k\rho)_0^2$ falls in the interval [0.00333; 0.1], resulting in local quasineutrality ranging from 10^{-4} to 10^{-2}.

Finally, the applicability of the algebraic model and the suggested optimal value of the parameter $(k\rho)_0^2$ should be regarded as estimates that are specific to this test problem rather than rigorously derived conclusions. This is primarily due to the fact that the dispersion relation in Eq. (17) was derived under the assumption of constant density and temperature. The same assumption was employed in the numerical tests presented in Sec. III C. Consequently, in more complex simulations where plasma parameters exhibit significant spatial and temporal variations, the optimal value of $(k\rho)_0^2$ may also vary accordingly.

IV. LOGICAL SHEATH

A. Formulation

The divertor target plates serve as absorbers of plasma particles and heat, and in this simplified model, they are represented as *fully absorbing* boundary conditions. Specifically, this entails the assumption that upon contact with the boundary, every particle is absorbed, and no new particles are introduced into the system thereafter. Consequently, rapid electron escape from the domain occurs at significantly faster rates, leading to the formation of a boundary sheath potential ϕ_{sh}. This potential prevents further electron escape and maintains global plasma quasineutrality. Achieving accurate numerical resolution of the boundary sheath layer presents notable computational challenges, given that the spatial and temporal scales of the sheath are orders of magnitude smaller than that of the plasma bulk. Furthermore, given the algebraic model adopted for the electrostatic potential in this context, which lacks sensitivity to small-scale spatial features, achieving precise treatment of the boundary becomes inherently unfeasible.

To address this challenge, reduced models are introduced in a way that they capture important physical effects and omit all the sheath complexity at the same time. One such model, explored in the current study, is the logical sheath boundary condition.[30] This boundary condition is designed to manipulate the ingoing electron fluxes so that the total normal boundary currents of electrons and ions are balanced, thus upholding global quasineutrality. Achieving equilibrium between electron and ion currents is accomplished by replicating the behavior of the sheath potential, where slow electrons are reflected and only fast electrons are permitted to exit the system. Importantly, the LSBC eliminates the need for resolving the boundary sheath potential, enabling significant simulation speed-up.

To simplify the discussion of the LSBC, we examine a modified version of Eq. (5) without any sources and collisions, incorporating some relabeling for clarity: $y \to x$, which is the coordinate in the configuration space, and $v_\parallel \to v$, which is the coordinate in the velocity space, respectively. The result is the 1D1V Vlasov equation in the conservative form,

$$\frac{\partial f}{\partial t} + \frac{\partial}{\partial x}(vf) + \frac{\partial}{\partial v}(\dot{v}f) = 0. \tag{26}$$

Without loss of generality, we assume that the boundary is located at $x = 0$ and the plasma is at $x > 0$. The total particle flux through the boundary is

$$\Psi = \int_{-\infty}^{0} f(x=0,v)\ v dv + \int_{0}^{\infty} f(x=0,v)\ v dv, \tag{27}$$

where integration in Eq. (27) is split to the two parts (from $-\infty$ to 0 and from 0 to ∞) to represent the outgoing and ingoing fluxes, respectively. Conservation of the total charge in the system implies that

$$q_i\Psi_i + q_e\Psi_e = 0, \tag{28}$$

which becomes $\Psi_i - \Psi_e = 0$ for singly-ionized ions. For the standard sheath BC, where electrons are reflected and ions are absorbed, the absorbing ion BC leads to $f_i(x=0, v>0) = 0$, and the charge conservation condition combined with Eq. (27) reads as

$$\int_{-\infty}^{0} f_i(0,v)\ v dv = \int_{-\infty}^{0} f_e(0,v)\ v dv + \int_{0}^{v_{esc}} f_e(0,v)\ v dv. \tag{29}$$

Here, v_{esc} represents the escape velocity, acting as a threshold determining whether electrons surpass or are reflected by the boundary. From that, the sheath potential can be defined as $\phi_{sh} = m_e v_{esc}^2/2$, and application of the LSBC involves determining the value of this potential at each time step.

Several important observations are noteworthy here. First, up to implementation details, the formulation of the LSBC discussed in this context can be adopted for integration into any continuum finite volume code framework, as it relies solely on the Vlasov equation. Second, reflection of the electrons on the boundary is assumed to be elastic, or in other words, fully charge and energy conservative; therefore, $f_e(0,v) = f(0,-v)$ for $v < v_{esc}$. Finally, the integration limits in Eq. (29) can be extended to infinity, provided that the electron and ion PDFs are zero on the boundary at $v > 0$ for ions and $v > v_{esc}$ for electrons. As a result, implementation of the LSBC can be achieved by precisely enforcing this requirement for the PDF, as elaborated in the subsequent section.

B. Implementation of LSBC

In the finite volume code COGENT, Eq. (26) is discretized on a grid in the computational space. The computational domain spans from 0 to x_{max} in the configuration space and from v_{min} to v_{max} in the velocity space. The grid is uniformly spaced in both dimensions, with spacings h_x and h_v in the configuration and velocity spaces, respectively, leading to the following relations for the number of cells $h_x N_x = x_{max}$, $h_v N_v = v_{max} - v_{min}$. The *cell-averaged* distribution function f is defined in every cell as $f_{i,j}$, where i is the configuration index, and j is the velocity index, as illustrated in Fig. 4. The difference between cell-averaged and cell-centered PDF is important when stencils for high order operations are derived[31] (in this work, for the third order advection scheme), and it reads as

$$f_{ca} = f_{cc} + \frac{h_x^2}{24} f''_{xx} + \frac{h_v^2}{24} f''_{vv}, \tag{30}$$

where "ca" stands for "cell-averaged," "cc" stands for "cell-centered," and f''_{dd} denotes the second derivative of f_{cc} in the direction of averaging d. In this work, the PDF is assumed to be cell-averaged; thus, the subscript "ca" is omitted for better readability. According to Eq. (26),

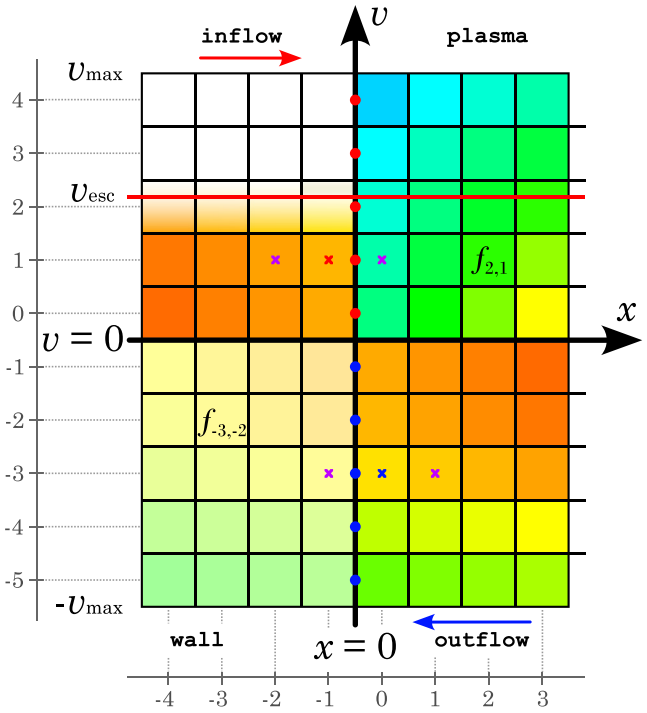

FIG. 4. Computational domain and ghost cells at the lower boundary $x = 0$. Ghost cells at $x < 0$ and $v < 0$ are filled by the polynomial extrapolation from the computational domain. Ghost cells at $x < 0$ and $v > 0$ are filled in a way that the LSBC is enforced.

the rate of change of f in a given cell or sub domain is equal to the negative total flux of f through all the boundaries. By definition, the total boundary flux Ψ is the integral over the boundary surface of the product of the normal component of the phase space velocity and the distribution function, which is exactly what is used in Eq. (29) to construct the LSBC. The flux through one cell boundary at $x = 0$ and velocity limits v_0 and v_1 reads as

$$\Psi = \int_{v_0}^{v_1} f(x = 0, v)\ v dv. \tag{31}$$

Using the Taylor expansion of f and the following variable transformations $2v_c = v_0 + v_1$, $\bar{v} = v - v_c$, and $\Delta v = v_1 - v_0$, we rewrite Eq. (31) as

$$\begin{aligned}\Psi = \int_{v_0}^{v_1} f(0, v)\ v dv &= \int_{-\Delta v/2}^{\Delta v/2} \left[f(0, v_c) + f'(0, v_c)\bar{v} \right](\bar{v} + v_c) d\bar{v} + O(\Delta v^3) \\ &= f(0, v_c) v_c \Delta v + \left(f(0, v_c) + v_c f'(0, v_c) \right) \int_{-\Delta v/2}^{\Delta v/2} \bar{v} d\bar{v} + O(\Delta v^3) \\ &= f(0, v_c) v_c \Delta v + O(\Delta v^3),\end{aligned} \tag{32}$$

where the integral of $\bar{v} d\bar{v}$ is zero due to the symmetry of integration and the integral of $\bar{v}^2 d\bar{v}$ results higher order corrections $O(\Delta v^3)$, which are later omitted. As follows from Eq. (32), the cell-centered approximation for the flux given by the expression $\Psi = f(x, v_c) v_c \Delta v$ is second order accurate with respect to grid spacing Δv. The total boundary flux from Eq. (29) can be computed as the sum of the individual fluxes on the boundary using Eq. (32), where face centered velocity values are given by

$$v_k = v(k) = v_{\min} + \frac{h_v}{2} + h_v (k - k_{\min}), \tag{33}$$

and the index k runs from $k_{\min}$ to $k_{\min} + N_v - 1$. If k_0 is such that $v_{k_0} \le 0$ and $v_{k_0+1} > 0$, then the second order accurate value of the outgoing ion flux I_i reads as

$$I_i = \int_{-\infty}^{0} f_i(0, v)\ v dv = h_v \sum_{k_{\min}}^{k_0} f_i(x = 0, v_k) v_k. \tag{34}$$

Here, we assume that the line $v = 0$ lies exactly on the cell boundary as shown in Fig. 4 in order to avoid unnecessary complexity associated with cells being split by the $v = 0$ level. The outgoing electron flux I_e is computed in the same way as I_i with the only exception of different h_v and v_k, as the velocity grid is usually renormalized to better capture features of electron PDF. Calculation of the ingoing electron flux J_e requires additional efforts, since v_{esc} is never on the cell boundary but instead it splits a cell marked with k^* index in the velocity space,

$$J_e = \int_{0}^{v_{esc}} f_e(0, v)\ v dv = h_v \sum_{k_0+1}^{k^*-1} f_e(0, v_k) v_k + \int_{v_{k^*} - h_v/2}^{v_{esc}} f_e(0, v)\ v dv. \tag{35}$$

The lower limit of integration in the last term in Eq. (35) corresponds to the velocity coordinate of the low boundary of the k^*-th cell, which we denote as v_{lo}. The upper boundary of this cell is $v_{hi} = v_{lo} + h_v$. The escape velocity splits this cell in the proportion ξ

$$\xi = \frac{v_{esc} - v_{lo}}{v_{hi} - v_{lo}} < 1. \tag{36}$$

Thus, the last term in Eq. (35) can be approximated as $\xi h_v f_e(0, v_{k^*})$. The error of this approximation is $O(h_v^2)$ that is yet consistent with the total error of J_e, because errors from every cell $O(h_v^3)$ are accumulated $O(N_v)$ times yielding $O(h_v^2)$ for the total error.

Exploiting the approach mentioned in the last paragraph of Sec. IV A together with Eqs. (34) and (35), one obtains values of the distribution function on the boundary $x = 0$ for all v_k as follows:

$$\begin{cases} f(0, v_k) = f(0, v_j), & \text{for } v_k = -v_j,\ k < k^*, \\ f(0, v_k) = \xi f(0, v_j), & \text{for } |v_k - v_{esc}| < h_v/2, \\ f(0, v_k) = 0, & \text{for } v_k > v_{esc} + h_v/2. \end{cases} \tag{37}$$

Equation (37) works for both species with the only exception that $v_{esc} = 0$ for ions implying full absorption, and v_{esc} is an unknown quantity for electrons that is found from the charge conservation in Eq. (29).

C. Filling of the ghost cells

Notice that $f(0, v_c)$ in Eq. (32) is the cell-centered value of the PDF on the face, which is calculated using cell-averaged data from nearby cells, depending on the order of the advection scheme. In this

work, we consider first and third order upwinding schemes, denoted as UW1 and UW3, with the following stencils for UW1:

$$\tilde{f}_{i+\frac{1}{2},j} = \begin{cases} f_{i,j}, & v > 0, \\ f_{i+1,j}, & v < 0, \end{cases} \tag{38}$$

and UW3, respectively,[32]

$$\tilde{f}_{i+\frac{1}{2},j} = \begin{cases} \frac{1}{6}\left(-f_{i-1,j} + 5f_{i,j} + 2f_{i+1,j}\right), & v > 0, \\ \frac{1}{6}\left(-f_{i+2,j} + 5f_{i+1,j} + 2f_{i,j}\right), & v < 0. \end{cases} \tag{39}$$

Here, $\tilde{f}_{i+\frac{1}{2},j}$ denotes the value of f on the cell face between cells with indices (i,j) and $(i+1, j)$. For example, $\tilde{f}_{-\frac{1}{2},1}$ is shown in Fig. 4 as a solid red dot on the boundary interface between two cells marked with purple and red crosses. Calculation of the face values of f for advection in the velocity direction is done similarly to Eqs. (38) and (39) with the only index swap $\tilde{f}_{i,j+\frac{1}{2}} \to \tilde{f}_{i+\frac{1}{2},j}$.

As it follows from Eqs. (37)–(39), calculation of the boundary fluxes necessitates values of the PDF in the ghost cells at $x < 0$. Filling ghost cells in the region $(x < 0, v < 0)$ is rather straightforward. These values are found via extrapolation from the computational domain using a high-order polynomial function. Values of the PDF in the ghost cells at the region $(x < 0, v > 0)$ are computed based on the values of the PDF on the boundary cell faces, provided by Eq. (37). This constraint alone is enough to fill the ghost cells for UW1 advection scheme

$$\begin{cases} f_{-1,k} = f_{0,-k}, & \text{for } v_k > 0,\ k < k^*, \\ f_{-1,k} = \xi f_{0,-k}, & \text{for } |v_k - v_{\rm esc}| < h_v/2, \\ f_{-1,k} = 0, & \text{for } v_k > v_{\rm esc} + h_v/2. \end{cases} \tag{40}$$

Equation (40) assigns values of the ghost cells by mirroring in velocity space values of the PDF in the boundary cells of the computational domain.

The third order advection scheme employs multi-point stencils and, thus, it requires more ghost cells to be filled. For every $v_k > 0$, the values in the ghost cells satisfy the following constraint:

$$\tilde{f}_{-\frac{1}{2},k} = \frac{1}{6}(-f_{-2,k} + 5f_{-1,k} + 2f_{0,k}), \tag{41}$$

where the boundary value $\tilde{f}$ is taken from Eq. (37). One more equation to find unknown $f_{-2,k}$ and $f_{-1,k}$ can be derived from the fact that $\tilde{f}_{-\frac{1}{2},k}$ can be also found by

$$\tilde{f}_{-\frac{1}{2},k} = \frac{1}{6}(-f_{1,k} + 5f_{0,k} + 2f_{-1,k}), \tag{42}$$

as if we reverse time and advect the PDF in the opposite direction. Equations (41) and (42) yield the solution

$$\begin{cases} f_{-1,k} = \frac{1}{2}\left(f_{1,k} - 5f_{0,k} + 6\tilde{f}_{-\frac{1}{2},k}\right), \\ f_{-2,k} = \frac{1}{2}\left(5f_{1,k} - 21f_{0,k} + 18\tilde{f}_{-\frac{1}{2},k}\right). \end{cases} \tag{43}$$

By design, Eq. (43) provides a third order accurate $O(h_x^3)$ solution for the PDF in the ghost cells. One may argue that the solution based on the counter propagation approach might be unstable as it explicitly makes use of the opposite direction stencil that is known to be unstable. While we did not do a precise stability analysis of Eq. (43), we never encountered any instabilities in our numerical simulations; thus, we conclude that this approach is a viable way to handle the LSBC for UW3 advection scheme. An alternative way to prove it is by deriving the solution from considering the face value $\tilde{f}_{\frac{1}{2},k}$ that can be calculated using shifted version of Eq. (41) and by local values of the PDF, namely, $f_{0,k}$, $f_{1,k}$, and $\tilde{f}_{-\frac{1}{2},k}$. We verified that the alternative approach yields the same solution as in Eq. (43), and the details of the derivation are provided in Appendix.

V. ELM HEAT PULSE SIMULATIONS

A. Simulation setup

Simulations of the ELM heat pulse propagation are performed with the COGENT code based on key principles described in this manuscript. Specifically, the simulations incorporate three fundamental components: (i) the one-dimensional geometry elucidated in Sec. II A (ii) the algebraic model for the gyrokinetic Poisson equation expounded upon in Sec. III C, and (iii) the logical sheath boundary condition introduced in Sec. IV. While the geometric configuration is confined to one dimension, the computational domain spans four dimensions, incorporating two velocity dimensions—parallel velocity $v_\parallel$ and magnetic moment μ—in addition to the configuration dimensions x and y. Notably, physical quantities are restricted to variation along the y-direction, with the x-direction reserved solely for the verification of the absence of the perpendicular instability. The computational domain adopts a uniform grid with dimensions specified as follows: $N_x = 4$, $N_y = 128$, $N_{v_\parallel} = 128$, $N_\mu = 64$. The results are insensitive to N_x and converge rapidly with respect to N_μ. High resolution in N_y is required to realize fine features that can appear close to the boundary, and high resolution in $N_{v_\parallel}$ is essential for the effective implementation of the LSBC. The code is executed on a single node utilizing 32 central processing unit (CPU) cores, with a typical production run requiring approximately 1 day, depending on grid resolution and the time step. The computational time can be significantly reduced when the problem simplifies to a 1D2V configuration, specifically in y, $v_\parallel$, and μ space. Parameters of the simulations are provided in Table I, where COGENT normalization units for density, temperature, length and velocity are n_0, T_0, V_0, and L_0 respectively.

The source term in Eq. (5) and initial conditions for both species are taken from the works of Shi[19] and Pan[20] for the sake of fair comparison of the simulation results. The source term is modeled as the following function:

$$S_\alpha = g(t)S(y)F_M(v_\parallel, \mu, T_{s\alpha}). \tag{44}$$

Here, $g(t)$ is the time dependent amplitude factor such that $g(t) = 1$ for $t < 200\,\mu$s and $g(t) = 1/9$ for $t > 200\,\mu$s, representing two stages of the ELM crash with intense heat occurring for first 200 μs and relaxation immediately after. The Maxwellian function $F_M(v_\parallel, \mu, T_s)$ for species α is determined by the temperature $T_{s\alpha}$ with

$$T_{si} = \begin{cases} 1.5\,\text{keV} & 0 \le t \le 200\,\mu\text{s}, \\ 0.26\,\text{keV} & t > 200\,\mu\text{s}, \end{cases} \tag{45}$$

$$T_{se} = \begin{cases} 1.5\,\text{keV} & 0 \le t \le 200\,\mu\text{s}, \\ 0.21\,\text{keV} & t > 200\,\mu\text{s}. \end{cases} \tag{46}$$

The shape profile in Eq. (44) is defined as

$$S(\bar{y}) = S_0 \cos\left(\frac{\pi\bar{y}}{2L_s}\right) H(L_s - |\bar{y}|), \tag{47}$$

where $\bar{y} = y - L_0/2$ is the domain centered coordinate, $2L_s$ is length of the source along the magnetic field line projected to the y-direction, and H is the Heaviside step function. The amplitude $S_0 = 9.066 \cdot 10^{23}\,\mathrm{m}^{-3}\mathrm{s}^{-1}$.

Initial conditions for electrons are characterized by constant temperature $T_{e0} = 75\,\mathrm{eV}$ and the following profile for density:

$$\frac{n_{e0}}{n_0} = 0.7 + 0.3\left(1 - \frac{2|\bar{y}|}{L_0}\right) + 0.5\cos\left(\frac{\pi\bar{y}}{2L_s}\right) H(L_s - |\bar{y}|). \tag{48}$$

The initial ion distribution function is represented as a combination of two half-Maxwellian distributions, namely,

$$f_{i0} = \begin{cases} F_L, & \bar{y} < -L_s, \\ \left(1 - \dfrac{\bar{y}}{L_s}\right)\dfrac{F_L}{2} + \left(1 + \dfrac{\bar{y}}{L_s}\right)\dfrac{F_R}{2}, & -L_s < \bar{y} < L_s, \\ F_R, & \bar{y} > L_s, \end{cases} \tag{49}$$

where left and right Maxwellian functions are defined as

$$F_{L,R}(\bar{y}, v_\parallel, \mu, T_{i0}) = 2n_{i0}(\bar{y}) F_M(v_\parallel, \mu, T_{i0}) H(\pm v_\parallel). \tag{50}$$

The initial ion density in Eq. (50) is identical to the initial electron density to guarantee exact global charge conservation that is enforced throughout simulations by the logical sheath boundary condition. The ion temperature profile is as follows:

$$\frac{T_{i0}}{T_0} = 1 + 0.45\left(1 - \frac{2|\bar{y}|}{L_0}\right) + 0.3\cos\left(\frac{\pi\bar{y}}{2L_s}\right) H(L_s - |\bar{y}|). \tag{51}$$

It is worth mentioning that the initial ion distribution function aligns with the absorbing boundary condition, which dictates no inflow at the boundary, thereby enforcing a zero PDF values at $y = 0$ and $v_\parallel = 0$. Conversely, under alternative circumstances, consistency emerges on transit time scales, leading to the emergence of electrostatic shear Alfvén wave structures propagating from the boundaries. Past studies have explored a smooth version of the source and initial plasma profiles, wherein the sharp Heaviside step function multiplied by a cosine function is substituted with a decaying exponential function. However, neither previous investigations nor our current study have discerned significant disparities between these two initial conditions; thus, the findings presented herein exclusively pertain to the sharp profiles.

B. Simulation results

A series of simulations were conducted employing UW1 and UW3 advection schemes across varied values of the $(k\rho)_0^2$ parameter, spanning 0.01–0.1. In all scenarios, the total charge within the system was consistently conserved up to $\sim 10^{-4}$ throughout the duration of the simulations. However, it is noteworthy that the absence of machine precision conservation arises from the leakage of the PDF through the velocity boundary of the computational domain. While this issue could potentially be alleviated by augmenting the resolution in the $v_\parallel$ space and achieving finer resolution of the exponential Maxwellian tails of electron and ion PDFs, such endeavors did not yield improved results and instead imposed a considerable computational burden on efficiency of the simulations.

Simulations employing the first-order advection scheme proved to be impractical due to significant numerical heating and dispersion resulting from the low-order approximation, leading to unrealistic electron heating on the ion acoustic time scales that it takes for the ELM pulse to arrive at the target plate. Specifically, the total parallel heat flux observed was nearly double that reported in prior studies. Additionally, the poor convergence rate rendered it nearly infeasible to conduct adequate simulations utilizing the UW1 advection scheme. Consequently, our focus shifted to the third-order UW3 advection scheme, which was subsequently employed for all simulations.

Before delving into the discussion of simulations employing the third-order advection scheme, it is worth mentioning that we also experimented with other approaches that did not require the complicated third-order LSBC. One such approach involved using a hybrid advection scheme, which applied the first-order method at the boundary and the third-order method elsewhere in the bulk. While this approach maintained relative simplicity in implementation and produced reasonable results, it suffered from inconsistencies in the fluxes at the interface between the first and second cells from the boundary. This inconsistency caused some unphysical jumps in the electron heat flux at the target plate when the ELM source was turned off.

The primary challenge associated with the third-order advection scheme relates to Gibbs oscillations, which manifest when the probability distribution function exhibits sharp features or jumps. In our model, such jumps are inevitable in both velocity and configuration spaces. In velocity space, the jump occurs at the escape velocity v_{esc}, where the PDF transitions to zero over a single cell size. In configuration space, inconsistencies between the PDF in the ghost cells and the computational domain lead to jumps as well. The Gibbs phenomenon results in the emergence of negative PDF values, exacerbating sharp gradients, which is shown in Figs. 5(a) and 5(c). Several approaches can mitigate this issue. One method, employed by Pan,[20] involves utilizing the non-oscillatory ENO/WENO advection scheme[33] and constructing a layered structure at the boundary that merges multiple advection schemes of varying orders. However, this approach is challenging to implement and compromises the high-order WENO5 approximation upon transitioning to UW1 at the boundary. Another approach is positivity preservation, a routine in COGENT that eliminates negative PDF values using nearby cells. While effective, this approach violates total charge conservation, resulting in deviations of a few percent over the simulation time frame. In the current work, we adopt a third approach, which introduces weak energy-conservative collisions employing the Dougherty drag-diffusion collision operator[34,35] that gradually transition the PDF to a Maxwellian distribution on ion acoustic time scales. This strategy helps prevent sharp features and negative PDF values without significantly altering the distribution function in the plasma bulk. Figures 5(a) and 5(b) demonstrate the ion PDF at $t = 200\,\mu s$ on the target plate in collisionless and weakly collisional cases. Sharp spikes of negative values observed in the collisionless case are mitigated when collisions are included. Notably, analogous plots for electron distribution functions depicted in Figs. 5(d) and 5(e) do not exhibit Gibbs oscillations or sharp gradients. A plausible explanation for this observation is that the oscillations are mitigated by the rapid transit dynamics of the electrons.

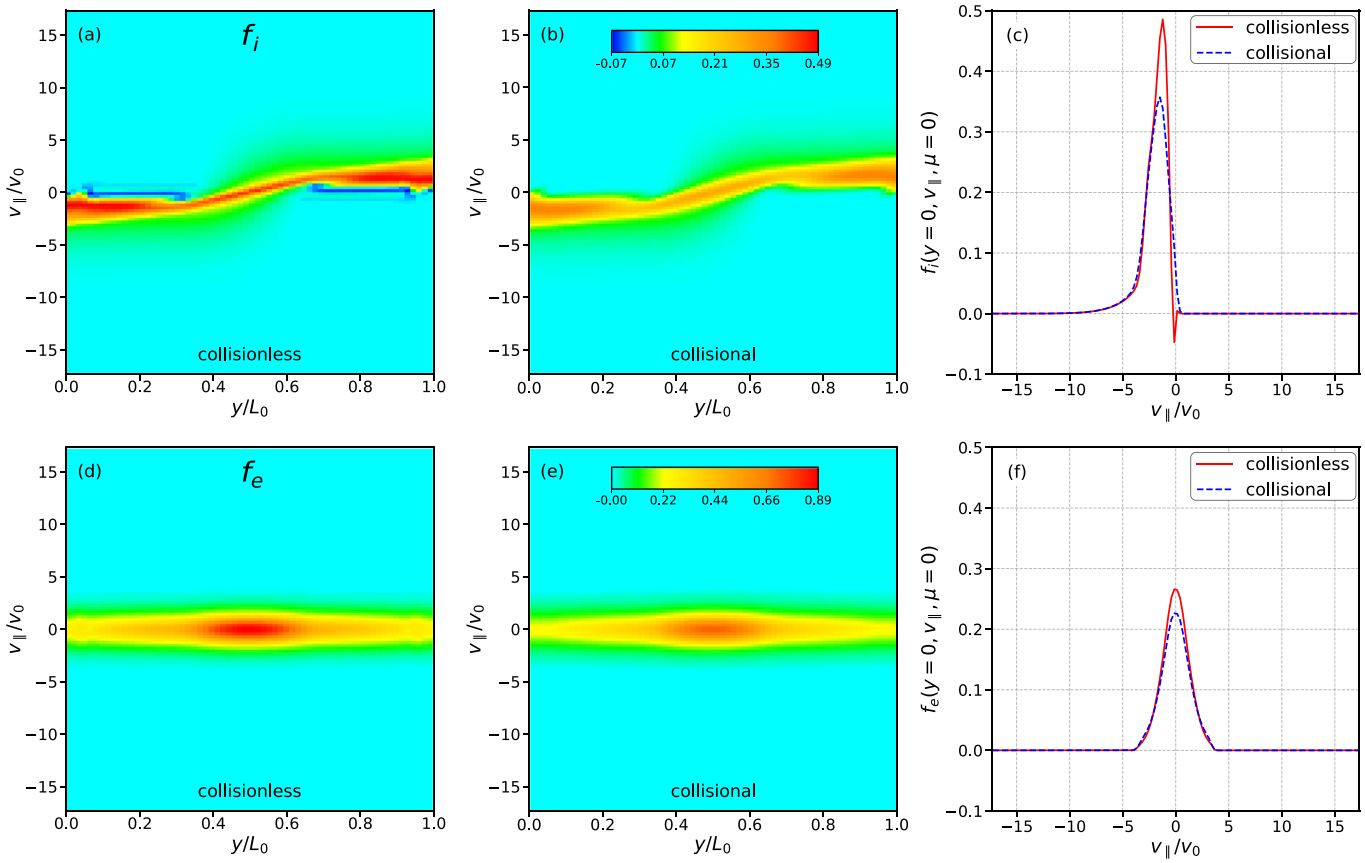

FIG. 5. Top row: comparison of the ion distribution functions at the divertor plate at $t = 200\ \mu$s in collisional ($c_e = 0.01$, $c_i = 0.01$) and collisionless cases. (a) and (b) are y-$v_\parallel$ phase plots ($\mu = 0$ slices) of the PDFs, and they both use the same custom colormap for better visibility purpose. Gibbs oscillations in the collisionless case are represented by thin sharp stripes of negative values, which are shown with dark blue color. (c) Lineout plots of both PDFs at the target plate ($y = 0$), with solid red and dashed blue lines corresponding to collisionless and collisional cases, respectively. Bottom row: analogous plots but for the electron PDFs. (d) Collisionless case; (e) weakly collisional case; and (f) lineout plots at $y = 0$.

Scanning across the parameter space of the algebraic potential model parameter $(k\rho)_0^2$ did not reveal any significant discrepancies in the total target plate heat flux, in agreement with findings reported by previous researchers. However, simulations conducted with low values of $(k\rho)_0^2$ necessitate a reduction in the electron CFL number to mitigate instabilities induced by electrostatic shear Alfvén waves. Unlike the results presented in Table II, a CFL parameter of approximately 0.5 is required to maintain stability of simulations. These discrepancies arise from the fact that the maximum resolved velocity in the simulations exceeds that in the test outlined in Sec. III C, resulting in a smaller stable CFL number.

Total parallel heat flux for species α is defined as follows:

$$Q_\alpha = \frac{m_\alpha}{2}\int_{-\infty}^{\infty} f_\alpha v_\parallel^3 dv_\parallel + (T_{\alpha\perp} + q_\alpha \phi_{\rm sh})\int_{-\infty}^{\infty} f_\alpha v_\parallel dv_\parallel, \qquad (52)$$

where f_α and $T_{\alpha\perp}$ are the PDF and perpendicular temperature on the boundary. The integration limits in Eq. (52) are different from those in the works of Shi and Pan, in particular, no escape velocity is involved in calculations. The reason is that the LSBC in the present work is constructed in a way that it automatically enforces a cut off at $v_{\rm esc}$ by setting the PDF values to zero. The term proportional to $q_\alpha\phi_{\rm sh}$ is the correction due to the accelerating/decelerating effect of the sheath potential $Q_{\rm sh}$. It does not impact the total target plate heat flux, since ion and electron particle fluxes are the same; however, it noticeably changes the fluxes of the individual species. The present results for the heat fluxes are in decent agreement with ones obtained from Gkeyll (see Fig. 3 in Ref. 19) and GENE (see Fig. 2 in Ref. 20).

The simulations were performed for $(k\rho)_0^2 = 0.04$, UW3 advection scheme, with weak collisions introduced for both species. The strength of collisions was controlled by a parameter c_α, which is a numerical coefficient in front of the Drag-Diffusion operator in the right hand side of Eq. (5). The value of c_α was chosen in a way that the simulation results for heat fluxes and the sheath potential are close to the original collisionless ones. The temporal evolution of divertor plate heat fluxes is illustrated in Fig. 6. Notably, a rapid increase in the electron heat flux occurs at approximately 1.2 μs, corresponding to $\tau_e/4$, where $\tau_e = L/\sqrt{T_e/m_e}$ denotes the electron transit time. Subsequently, the ion heat flux remains relatively low, only experiencing slight corrections due to the sheath potential, until the arrival of

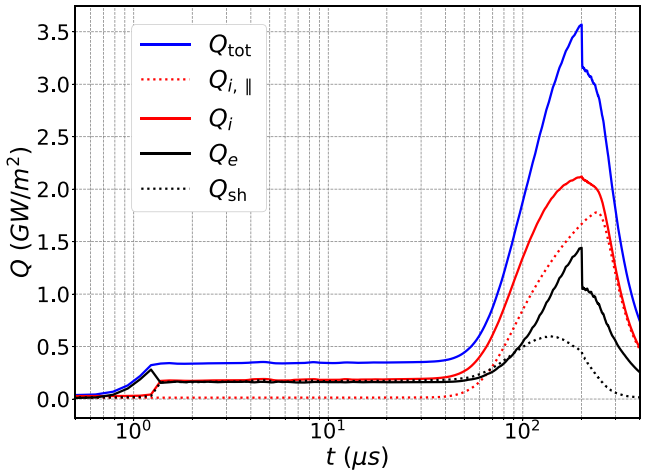

FIG. 6. Total parallel heat flux on the target plate. Dotted red: parallel ion heat flux $Q_{i,\parallel}$ before entering the sheath region. Solid red: ion heat flux Q_i adjusted by the sheath potential impact. Solid black: electron heat Q_e adjusted by the sheath potential. Dotted black: boundary sheath correction Q_{sh}. Blue: total Q_{tot} heat flux on the target plate.

hot ions from the ELM source at approximately 70 μs, equivalent to a quarter of the ion transit time. Following this, both fluxes exhibit growth until the conclusion of the ELM heating period at 200 μs, followed by a gradual decay over the ion transit time. The observed peak heat flux around 3.6 GW/m^2 is approximately 10% lower than reported in previous studies, but a value of 4 GW/m^2 in good agreement with previous results is obtained when using higher electron collisionality. A comparison of the effects of collisionality relative to numerical dissipation is out of the scope of the present work and will be explored in the future.

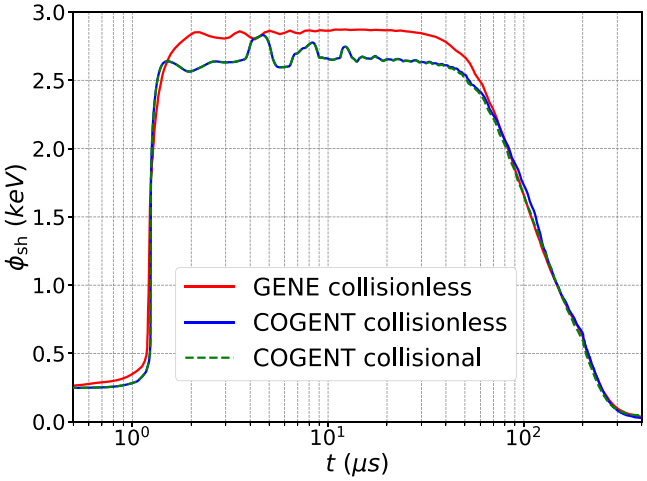

FIG. 7. Temporal evolution of the sheath potential. Red: GENE[20] collisionless run[a]; blue: COGENT collisionless run; dashed green: COGENT collisional ($c_e = 0.01$, $c_i = 0.01$) run. In both COGENT simulations, UW3 advection scheme and $(k\rho)_0^2 = 0.04$ were used. [a]The data are obtained from Fig. 3 in Ref. 20 by using a data extractor script, therefore, errors on the order of the linewidth are possible.

The evolution of the sheath potential ϕ_{sh} is depicted in Fig. 7. In this analysis, we compare our findings from both collisional and collisionless models with those presented in the work of Pan.[20] Notably, the rapid growth and subsequent plateauing of ϕ_{sh} closely mirror the behavior observed in the electron heat flux. However, a disparity between COGENT simulations and Pan's results is the more pronounced oscillatory nature of the plateau region in COGENT simulations. These oscillations correspond to electrostatic Alfvén wave interactions with the domain boundary and are absent in Pan's results, where initial conditions were set to ensure Boltzmann equilibrium between electrons and ions, thereby minimizing subsequent oscillations. The other notable discrepancy is in amplitude of the sheath potential at the plateau region that might be speculated is due to different numerical implementations of the LSBC in GENE and COGENT. As previously mentioned, collisions for both species are weak, resulting in minimal discrepancies between collisional and collisionless cases in the temporal evolution of the sheath potential.

VI. CONCLUSIONS

Simulations of ELM heat pulse propagation in the scrape-off layer of the tokamak were conducted utilizing the gyrokinetic code COGENT. Adopting a simplified 1D geometry and leveraging simulation parameters from prior studies facilitated a fair comparison and validation of our results. Notably, our findings exhibit favorable agreement with previous kinetic and gyrokinetic simulations, both in terms of the electron and ion heat flux magnitudes, as well as their temporal dynamics. To ensure the robustness and consistency of our findings, we conducted a series of simulations employing various settings. This encompassed parameter and resolution scans, as well as the utilization of both collisional and collisionless models.

In this study, we focused on two crucial elements of our model: the algebraic simplification for the electrostatic potential and the logical sheath boundary condition. Our investigation into the algebraic model involved a comprehensive assessment of its applicability, considering local quasineutrality and the potential for numerical instability induced by electrostatic shear Alfvén waves. Through linear analysis and the examination of ESAW propagation, we identified an optimal parameter range within the model's parameter space. This range significantly enhances simulation speed while maintaining fidelity to underlying physical processes.

The logical sheath boundary condition underwent a comprehensive examination for the third order upwinding advection scheme, which, to the best of our knowledge, had not been thoroughly explored in prior literature. A focal point of this investigation was the proper handling of ghost cells, a crucial aspect of the LSBC to ensure consistency with the advection scheme utilized in the code. Our analysis revealed both advantages and challenges associated with various advection schemes, encompassing issues like excessive numerical heating and diffusion in first-order advection, and the Gibbs phenomenon in higher-order schemes like the third order UW3. Notably, the current implementation of the LSBC is adaptable to any finite volume code, not limited to gyrokinetic models. While our research provides advancement in understanding the LSBC, further studies are warranted to extend its applicability to higher-order schemes and non-oscillatory advection methods, such as WENO5.

Future research on the problem of ELM heat pulse propagation should encompass extensions to two-dimensional or three-dimensional geometries, including the complex geometries found in

the scrape-off layer of tokamaks. To thoroughly address these extensions, the models developed in the present work must be reevaluated, and, if necessary, replaced with more advanced alternatives. For instance, the algebraic model for the electrostatic potential may not be easily adaptable due to significant discrepancies in parallel and perpendicular scales within the SOL. Additionally, the steady-state model for ELM heat pulses could be superseded by a self-consistently calculated transport model once collisions and turbulence are adequately incorporated. The development of an advanced logical sheath boundary condition that incorporates various divertor configurations, as well as plasma-surface interactions such as recycling and secondary electron emission, may be of particular interest.

ACKNOWLEDGMENTS

This work was prepared by LLNL for U.S. DOE SC-FES (Contract No. DE-AC52-07NA27344) and was supported by DOE Office of Science, Office of Fusion Energy Sciences and Office of Advanced Scientific Computing Research, through the SciDAC project on Plasma-Surface Interactions.

AUTHOR DECLARATIONS

Conflict of Interest

The authors have no conflicts to disclose.

Author Contributions

V. I. Geyko: Conceptualization (equal); Data curation (equal); Formal analysis (equal); Investigation (equal); Methodology (equal); Software (equal); Validation (equal); Visualization (equal); Writing – original draft (equal); Writing – review & editing (equal). **I. Joseph:** Conceptualization (lead); Formal analysis (equal); Funding acquisition (equal); Methodology (equal); Project administration (lead); Supervision (equal); Writing – review & editing (equal). **M. A. Dorf:** Conceptualization (equal); Formal analysis (equal); Project administration (supporting); Software (equal); Writing – review & editing (equal). **D. Ghosh:** Formal analysis (supporting); Software (supporting); Validation (supporting); Writing – review & editing (supporting). **M. R. Dorr:** Software (equal); Validation (equal); Writing – review & editing (equal).

DATA AVAILABILITY

The data that support the findings of this study are available from the corresponding author upon reasonable request.

APPENDIX: FLUX BASED DERIVATION OF THE LSBC FOR THE THIRD ORDER ADVECTION SCHEME

One can notice that the value of the distribution function on the face with label $1/2$ can be found either using stencil points $\{-1, 0, 1\}$ and employing Eq. (41) as

$$\tilde{f}_{\frac{1}{2},k} = \frac{1}{6}(-f_{-1,k} + 5f_{0,k} + 2f_{1,k}), \tag{A1}$$

or using the PDF value on the face labeled $-1/2$ and two nearby cell-averaged values $f_{0,k}$ and $f_{1,k}$. To that end, we consider the second order Taylor expansion of f around the face labeled $1/2$, namely,

$$f(x) = \tilde{f}_{\frac{1}{2},k} + f'_k x + f''_k \frac{x^2}{2} + O(x^3), \tag{A2}$$

where derivatives f'_k and f''_k are calculated at $x = h_x$. Ignoring higher order terms, it follows from Eq. (A2) that

$$\tilde{f}_{-\frac{1}{2},k} = \tilde{f}_{\frac{1}{2},k} - f'_k h_x + f''_k \frac{h_x^2}{2}. \tag{A3}$$

By definition of a cell-averaged quantity, integrals of Eq. (A2) with respect to x from 0 to $\pm h_x$ are equal to cell-averaged values $f_{0,k}$ and $f_{1,k}$ multiplied by the cell length h_x. These integrals yield the following equations:

$$\begin{cases} f_{0,k} = \tilde{f}_{\frac{1}{2},k} - f'_k \frac{h_x}{2} + f''_k \frac{h_x^2}{6}, \\ f_{1,k} = \tilde{f}_{\frac{1}{2},k} + f'_k \frac{h_x}{2} + f''_k \frac{h_x^2}{6}. \end{cases} \tag{A4}$$

The system of three linear Eqs. (A3) and (A4) has three unknown variables: f'_k, f''_k, and $\tilde{f}_{\frac{1}{2},k}$. Skipping simple algebra, one can find the solution as

$$\tilde{f}_{\frac{1}{2},k} = \frac{1}{4}\left(5f_{0,k} + f_{1,k} - 2\tilde{f}_{-\frac{1}{2},k}\right). \tag{A5}$$

Equation (A1) combined with Eq. (A5) yields the expression for $f_{-1,k}$,

$$f_{-1,k} = \frac{1}{2}\left(-5f_{0,k} + f_{1,k} + 6\tilde{f}_{-\frac{1}{2},k}\right), \tag{A6}$$

which is identical to Eq. (A3) used in Sec. IV C, hence concluding the derivation.

REFERENCES

[1]F. Wagner, G. Becker, K. Behringer, D. Campbell, A. Eberhagen, W. Engelhardt, G. Fussmann, O. Gehre, J. Gernhardt, G. V. Gierke *et al.*, Phys. Rev. Lett. **49**, 1408 (1982).
[2]R. J. Groebner, Phys. Fluids B **5**, 2343 (1993).
[3]H. Zohm, Plasma Phys. Controlled Fusion **38**, 105 (1996).
[4]S. Clement, A. Chankin, D. Ciric, J. Coad, J. Falter, E. Gauthier, J. Lingertat, and S. Puppin, J. Nucl. Mater. **266–269**, 285 (1999).
[5]A. W. Leonard, T. H. Osborne, M. E. Fenstermacher, R. J. Groebner, M. Groth, C. J. Lasnier, M. A. Mahdavi, T. W. Petrie, P. B. Snyder, J. G. Watkins, and L. Zeng, Phys. Plasmas **10**, 1765 (2003).
[6]M. Becoulet, G. Huysmans, P. Thomas, E. Joffrin, F. Rimini, P. Monier-Garbet, A. Grosman, P. Ghendrih, V. Parail, P. Lomas *et al.*, J. Nucl. Mater. **337–339**, 677 (2005).
[7]R. Pitts, P. Andrew, G. Arnoux, T. Eich, W. Fundamenski, A. Huber, C. Silva, D. Tskhakaya, and JET EFDA Contributors, Nucl. Fusion **47**, 1437 (2007).
[8]R. A. Pitts, J. P. Coad, D. P. Coster, G. Federici, W. Fundamenski, J. Horacek, K. Krieger, A. Kukushkin, J. Likonen, G. F. Matthews, and M. Rubel, Plasma Phys. Controlled Fusion **47**, B303 (2005).
[9]J. Coenen, G. Arnoux, B. Bazylev, G. Matthews, S. Jachmich, I. Balboa, M. Clever, R. Dejarnac, I. Coffey, Y. Corre *et al.*, J. Nucl. Mater. **463**, 78 (2015).
[10]J.-S. Lönnroth, G. Bateman, M. Bécoulet, P. Beyer, G. Corrigan, C. Figarella, W. Fundamenski, O. E. Garcia, X. Garbet, G. Huysmans *et al.*, Contrib. Plasma Phys. **46**, 726 (2006).
[11]E. Havlíčková, W. Fundamenski, V. Naulin, A. H. Nielsen, R. Zagórski, J. Seidl, and J. Horáček, Plasma Phys. Controlled Fusion **53**, 065004 (2011).
[12]A. Loarte, G. Saibene, R. Sartori, T. Eich, A. Kallenbach, W. Suttrop, M. Kempenaars, M. Beurskens, M. de Baar, J. Lönnroth *et al.*, Phys. Plasmas **11**, 2668 (2004).

[13]A. Bergmann, Nucl. Fusion **42**, 1162 (2002).
[14]T. Takizuka and M. Hosokawa, Contrib. Plasma Phys. **46**, 698 (2006).
[15]D. Tskhakaya, R. Pitts, W. Fundamenski, T. Eich, S. Kuhn, and JET EFDA Contributors, J. Nucl. Mater. **390–391**, 335 (2009).
[16]G. Manfredi, S. Hirstoaga, and S. Devaux, Plasma Phys. Controlled Fusion **53**, 015012 (2011).
[17]J. T. Omotani and B. D. Dudson, Plasma Phys. Controlled Fusion **55**, 055009 (2013).
[18]E. Havlíčková, W. Fundamenski, D. Tskhakaya, G. Manfredi, and D. Moulton, Plasma Phys. Controlled Fusion **54**, 045002 (2012).
[19]E. L. Shi, A. H. Hakim, and G. W. Hammett, Phys. Plasmas **22**, 022504 (2015).
[20]Q. Pan, D. Told, and F. Jenko, Phys. Plasmas **23**, 102302 (2016).
[21]I. Joseph, M. Dorf, and M. Dorr, Nucl. Mater. Energy **19**, 330 (2019).
[22]M. A. Dorf, R. H. Cohen, M. Dorr, T. Rognlien, J. Hittinger, J. Compton, P. Colella, D. Martin, and P. McCorquodale, Phys. Plasmas **20**, 012513 (2013).
[23]D. H. E. Dubin, J. A. Krommes, C. Oberman, and W. W. Lee, Phys. Fluids **26**, 3524 (1983).
[24]T. S. Hahm, Phys. Plasmas **3**, 4658 (1996).
[25]W. Lee, J. Comput. Phys. **72**, 243 (1987).
[26]E. Belli and G. Hammett, Comput. Phys. Commun. **172**, 119 (2005).
[27]W. W. Lee, J. L. V. Lewandowski, T. S. Hahm, and Z. Lin, Phys. Plasmas **8**, 4435 (2001).
[28]R. L. Lysak and W. Lotko, J. Geophys. Res. **101**, 5085, https://doi.org/10.1029/95JA03712 (1996).
[29]R. Courant, K. Friedrichs, and H. Lewy, IBM J. Res. Dev. **11**, 215 (1967).
[30]S. Parker, R. Procassini, C. Birdsall, and B. Cohen, J. Comput. Phys. **104**, 41 (1993).
[31]M. Barad and P. Colella, J. Comput. Phys. **209**, 1 (2005).
[32]Y.-T. Zhang and C.-W. Shu, *Handbook of Numerical Methods for Hyperbolic Problems*, Handbook of Numerical Analysis, Vol. 17, edited by R. Abgrall and C.-W. Shu (Elsevier, 2016), pp. 103–122.
[33]G.-S. Jiang and C.-W. Shu, J. Comput. Phys. **126**, 202 (1996).
[34]J. P. Dougherty and S. R. Watson, J. Plasma Phys. **1**, 317–326 (1967).
[35]J. R. Angus, "On anomalous plasma transport in the edge of magnetic confinement devices," Ph.D. thesis (University of California, San Diego, 2012).